SCIENCE CHINA
Technological Sciences

•Article•

November 2023 Vol.66 No.11: 3267–3275
https://doi.org/10.1007/s11431-023-2478-0

Large area crystalline Weyl semimetal with nano Au film based micro-fold line array for THz detector

SONG Qi[1], ZHOU Yu[2*], JIA ErSe[4], WANG JiaTong[3], ZHANG Min[3*] & ZHANG BingYuan[1*]

[1] Shandong Key Laboratory of Optical Communication Science and Technology, School of Physics Science and Information Technology, Liaocheng University, Liaocheng 252059, China;
[2] North China Institute of Computing Technology, Beijing 100083, China;
[3] Key Laboratory of Optoelectronic Devices and Systems of Ministry of Education and Guangdong Province, College of Physics and Optoelectronic Engineering, Shenzhen University, Shenzhen 518060, China;
[4] School of Precision Instrument and Opto-electronics Engineering, Tianjin University, Tianjin 300072, China

Received June 10, 2023; accepted July 28, 2023; published online September 8, 2023

The advancement of 6G technology relies on the development of high-performance terahertz detectors that can operate at room temperature. These detectors are crucial for Internet of Things (IoT) applications, which require sensitive environmental sensing and efficient reception of 6G signals. One significant research focus is on detection technology with high responsiveness and low equivalent noise power for 6G signals, which experience high losses in the air. To meet the demand for ultra-sensitive detectors in 6G technology, we have employed several techniques. Firstly, we prepared a large area of Weyl-semimetal layer through magnetron sputtering. Secondly, we obtained a high-quality Weyl-semimetal active layer by carefully controlling the annealing conditions. Next, a thin nano-Au layer was introduced as a micro-cavity reflection layer to enhance the device's detection rate. Additionally, we incorporated an electromagnetic induction well to improve carrier confinement and enhance the detection sensitivity. This proposed high-performance terahertz detector, with its potential for industrial production, offers a valuable technical solution for the advancement of 6G technology.

micro-cavity, Weyl semimetal, crystalline thin film, THz device

Citation: Song Q, Zhou Y, Jia E S, et al. Large area crystalline Weyl semimetal with nano Au film based micro-fold line array for THz detector. Sci China Tech Sci, 2023, 66: 3267–3275, https://doi.org/10.1007/s11431-023-2478-0

1 Introduction

The maturity of Internet of Things (IoT) technology has led to significant growth in IoT-based system applications. This trend is particularly evident in various areas such as personal wearable devices, intelligent transportation systems for vehicle networking, and medical services to the financial industry. With the intelligent 6G technology offering advantages like broad bandwidth and high transmission rates, there are strong prospects for applying artificial intelligence (AI) at the network edge [1–3]. In this context, edge intelligence technology has emerged as a convergence of AI, communication, and edge computing technologies, enabling innovative solutions and facilitating efficient data processing at the network edge. The success of edge intelligence applications in 6G network technology relies on high-performance terahertz detectors. These detectors are essential for IoT scenarios, as they enable sensitive environmental sensing and efficient reception of 6G signals, which experience significant losses in the air. Therefore, it is crucial to research detection technology that offers high responsiveness and low equivalent noise power for 6G signals. This research focuses on optimizing the performance of terahertz detectors,

*Corresponding authors (email: zhouyu@cetcjt.com; zhangmin@szu.edu.cn; zhangbingyuan@lcu.edu.cn)

ensuring they can effectively capture and process weak 6G signals while minimizing noise interference [4–7].

The current sensitive detection technology of terahertz waves at room temperature includes the detection technology based on photoelectric signals and the detection technology based on thermoelectric signals. The detection technology based on thermoelectric signals utilizes the thermal effect caused by terahertz waves, resulting in changes in the phase change or electrical conductivity of the active layer material, enabling the detection of terahertz signals. The thermoelectric signal detection method generally has a slower detection rate. On the other hand, the photoelectric signal detection method utilizes the interaction between terahertz photons and the active layer material to generate photocurrent for detection. Due to the low energy of terahertz photons, materials with nearly zero band gap are required to induce photocurrent. Additionally, in order to reduce noise, the active layer materials should have strong absorption capabilities for low-energy photons. As a result, Weyl-semimetallic materials with topological Weyl-point energy band structures have been gaining attention from researchers [8–10].

The close-to-zero band gap of the Weyl semimetal energy band system allows it to effectively absorb terahertz waves with low photon energies. When THz waves are absorbed, the carriers in Weyl semimetal move towards the vicinity of the Weyl point. This leads to an enhanced displacement current response, which is associated with the diverging Berry curvature [11–13]. As a result, the Weyl semimetal exhibits an increased photocurrent response for terahertz waves with low photon energies. This makes it more suitable for detecting such terahertz waves with improved sensitivity and reduced noise compared to other materials [14]. To achieve a large area for efficient active layer preparation, magnetron sputtering was chosen as the active layer processing method. The carrier generation and transport efficiency increases dramatically after the crystallization of the film, and annealing is a more ideal crystallization method for magnetron-sputtered films [15]. We investigated the preparation of high-quality crystalline films using different annealing temperatures and different annealing times.

When subwavelength microstructures are added to the surface of the active layer, it can induce a localized surface plasmon (LSP) effect. This effect occurs when the incident signal, such as a 6G signal in the terahertz band, interacts with both the active layer material and the array of subwavelength microstructures on its surface. The interaction between the signal and the microstructures can lead to enhanced light-matter interactions, improved signal propagation, or other specific functionalities [16–18]. Adding subwavelength structures to the active layer can confine the THz wave (6G signal) to a small region, leading to enhanced contact between the signal and the active layer. This confinement greatly increases the photocurrent and improves the responsiveness of the detector. Laser direct writing technology allows for the creation of two-dimensional (2D) microstructures on the device surface with minimal limitations. It is capable of processing structures with line widths of approximately 20 microns, which is suitable for terahertz functional devices in terms of accuracy. Laser direct writing is a simple and cost-effective method for achieving precise surface patterns on the micron and 100-micron scale without the need for additional materials or causing additional losses. This technique is discussed in further detail as a viable approach for creating these patterns in the references provided. To increase the interaction between the terahertz field and the active layer in the smallest scale, a micro-cavity structure can be introduced to take advantage of the reflection of terahertz waves from the metal layer and the large number of free carriers in the metal layer, a micro-reflection cavity can be formed between the Weyl semi-metal layer and the metal layer, which can further enhance the detection effect of the device by re-incidence with the active layer after THz reflection. Therefore, we added a nanofilm Au layer in the design, as a reflection layer of terahertz waves can also collect carriers and increase the detected photocurrent. In addition, a subwavelength microstructure is prepared between the metal layer and the Weyl metal layer by femtosecond laser direct writing technique, and an electromagnetic induction well (EIW) is formed near the structure to transfer the carriers in the metal layer to the semimetal layer and confine them around the subwavelength structure, so that an EIW with confined carriers is formed around the half-metal microstructure, and this region where a large number of carriers gather changes the dielectric constant of the material itself, which is more sensitive to the incident terahertz wave. This region of massive carrier aggregation changes the dielectric constant of the material itself and makes it more sensitive to the response of incident terahertz waves, further increasing the detection efficiency of terahertz waves.

In summary, to realize the requirement of edge-smart ultra-sensitive detectors for 6G IoT technology, we have prepared large-area Weyl-semi-metal layers by magnetron sputtering, and obtained high-quality Weyl-semimetal active layers by controlled annealing conditions. Additionally, nanofilm Au layers were prepared as microcavity reflection layers to enhance the device detection rate. Finally, 2D surfaceized micropattern arrays were created using laser direct writing technique. The resulting terahertz detector is high-performance and has the potential for industrial production. Our devices have the potential to contribute to the development of edge intelligence for 6G IoT technology.

2 Experimental procedure

To obtain high-quality WTe_2 films, we followed a procedure involving the preparation of WTe_2 films on silicon substrates using magnetron sputtering. Subsequently, the devices were transferred to an annealing table that was protected by nitrogen gas. The devices were then heated to various temperatures and held for different durations to complete the annealing process. Finally, the annealing quality was assessed by characterizing the Raman spectra under different annealing conditions using Raman spectroscopy. The prepared film area is 5 mm × 10 mm. The thickness of Au layer and WTe_2 layer are 36 nm and 1.08 μm. The WTe_2 layer and Au layer were prepared by the following steps. At first, the air pressure was reduced to 9×10^{-4} Pa, and injects argon into the cavity. The WTe_2 target is coated using radio frequency (RF) drive mode, and the Au target is coated using direct current (DC) drive mode. For the WTe_2 layer, the parameters were set as follows. The argon flow rate of 50 standard cubic centimeter per minute (SCCM), power of 100 W, and duration time of 600 s was set. For the Au layer, the argon flow rate, current and duration time of 15 SCCM, 0.2 A, and 90 s were set. First, we characterized the properties of the films using X-ray photoelectron spectroscopy (XPS) in Figure 1(a) and (b), and the results showed that the $4p_1$ and 4s feature peaks of the W element of WTe_2 are located at 490.5 and 593.6 eV. The $3d_3$ and $3d_5$ feature peaks of the Te element are located at 583.3 and 572.9 eV. The thickness of Au layer and WTe_2 layer are shown in Figure 1 (c) and (d).

We conducted annealing experiments on WTe_2 films with the same coating parameters and thickness results using a nitrogen-filled gas annealing platform. The crystallization of the WTe_2 films was characterized at different annealing temperatures. By referring to the relationship between Raman spectra and crystallization provided in the literature [19,20] (see Figure 2(a)), it can be concluded that a narrower Raman peak position and a higher relative intensity indicate a better crystallization effect. Applying this principle, we determined that the optimal crystallization of the film is achieved at an annealing temperature of 150°C. However, as the temperature exceeds 200°C, the crystallization effect gradually diminishes. This decrease in crystallization may be attributed to the disruption of WTe_2 molecular bonds at high temperatures, resulting in poor crystallization.

Figure 2(b) displays the complex conductivity of the WTe_2 nanofilm at room temperature. To analyze the frequency dependence of conductivity, we employed the ordinary Drude equation for fitting purposes [21].

$$\sigma(\omega) = \sigma_0 \frac{1}{1 - i\omega\tau}, \tag{1}$$

where ω indicates the frequency of the THz wave, τ is the quasiparticle relaxation time, and σ_0 is DC conductivity. The results of the complex conductivity in the terahertz band show the best complex conductivity parameters at the preferred annealing temperature, i.e., 60 min at 150°C. The WTe_2 films obtained under this condition are more suitable for use as devices in the THz band.

The current probe platform and terahertz time-domain spectrum system are shown in Figure 3(a) and (b). Therefore, we chose to anneal the WTe_2 films prepared by magnetron sputtering at 150°C. In addition, we also selected the annealing time, and the best effect was obtained at 60 min.To

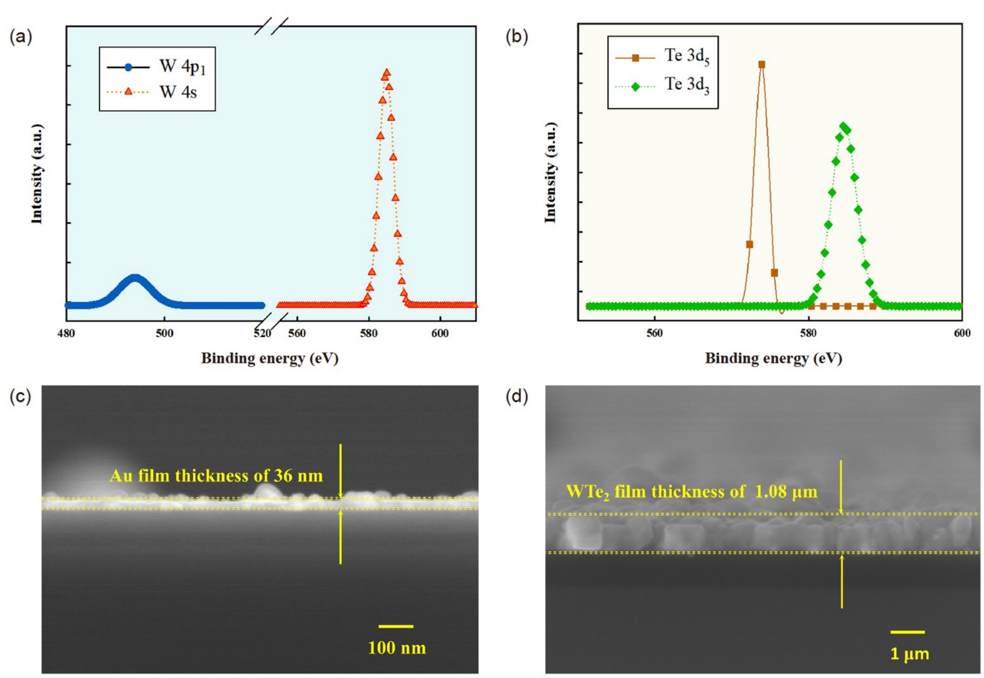

Figure 1 (Color online) Characterization of WTe_2 thin films. (a and b) XPS results of WTe_2 thin films. (c) SEM of Au film thickness. (d) SEM of WTe_2 film thickness.

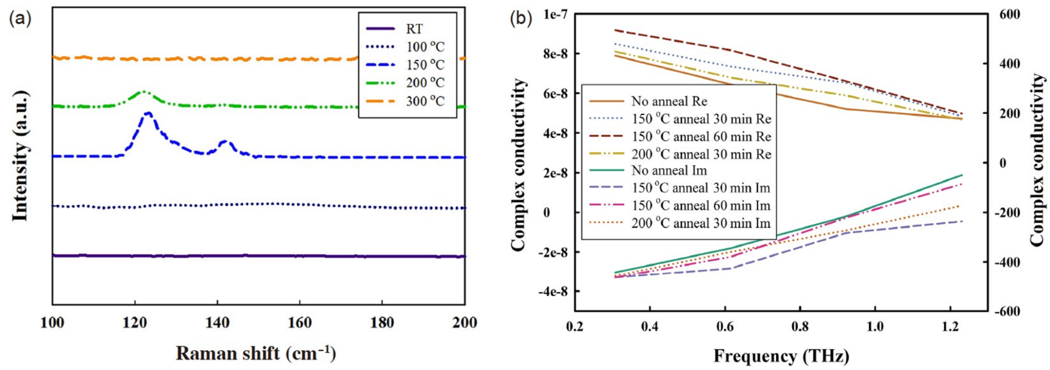

Figure 2 (Color online) Characterization results for different annealing temperatures. (a) Raman spectrum. (b) Complex conductivity in THz frequency.

further confirm the influence of crystalline films on terahertz detection after annealing, we tested the complex conductivity of several films with different annealing temperatures at the same annealing time in the terahertz frequency range. The test system is a photoconductive antenna (PCA) transmit and receive-based terahertz time-domain spectroscopy system. The THz beam was not focused on the sample. The laser used in our experiment with the central wavelength of 780 nm, the repetition frequency of 80 MHz, the pulse width of 90 fs, and the spectral width of 7 nm.

In the following, we prepared Au electrodes with the same pitch (3 mm) on crystalline thin film devices under different annealing conditions, respectively, used 0.1 THz source incidence, and examined the detection effect of the films on terahertz waves under different conditions.

We employed a method of comparing light and dark currents, utilizing light current excitation, to assess the detection capability of the device. The terahertz detector is positioned at the center of the probe platform, and two robust tungsten steel probes (with a needle tip size of 10 μm) are utilized to establish contact with the metal electrodes of the device. These probes are connected to a digital source meter, specifically the Keithley 2400. As for the terahertz emitter, we utilized terahertz IMPATT diodes, specifically the TeraSense IMPATT diodes model at 0.1 THz, with a maximum output power of 70 mW. Prior to the experiment, we measured the output power using a THz power meter (ELVA-1 DPM). It is worth noting that the total area of our device exceeds the diffraction-limited area.

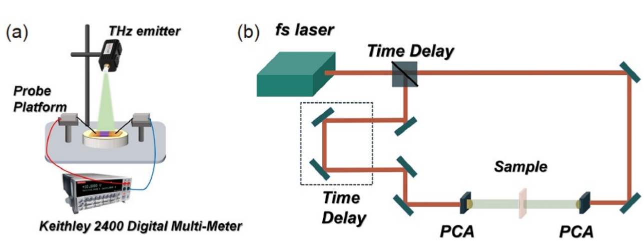

Figure 3 (Color online) Schematic diagram of the THz test system. (a) Current probe platform. (b) Terahertz time-domain spectrum system.

Figure 4 illustrates the detection performance, encompassing the total noise, responsivity, noise equivalent power (NEP), and detectivity (D^*) for the WTe_2 thin film devices under various annealing temperatures and times. Specifically, we consider the following annealing conditions: 150°C for 30 min, 150°C for 60 min, 200°C for 30 min, and an unannealed device as a reference. Based on the results of the detection experiments, it is evident that the annealing condition of 150°C for 60 min yields the most favorable outcomes. This aligns with the findings of the Raman characterization, as under this specific annealing condition, the film demonstrates more ideal crystallization, resulting in higher carrier mobility within the crystalline film of the same material. Consequently, this leads to a larger bright current and improved detection. Furthermore, the results indicate that annealing at 200°C for 30 min outperforms annealing at 150°C for the same duration. This can be attributed to the fact that high temperatures cause the breaking of certain molecular bonds, thereby enhancing detection at 150°C. To further demonstrate the photo-electrical conversion capability of their detectors, we also calculate the photoresponsivity (R_A), NEP, and D^* through a light-dark current comparison.

R_A, NEP, and D^* are defined as [22,23]

$$R_A = I / P,$$

$$\mathrm{NEP} = v_n / R_A,$$

and

$$D^* = \sqrt{S} / \mathrm{NEP}, \tag{2}$$

where I is the photocurrent of the device. P is the incident THz power, and S is the effective detection area of the detector. And v_n is the noise voltage as shown in Eq. (2) [23].

$$v_n = \sqrt{{v_t}^2 + {v_b}^2} = \sqrt{4k_B Tr + 2qI_d r^2}, \tag{3}$$

where k_B, T, r, q, and I_d are Boltzmann's constant, the detector's absolute temperature, resistance value, elementary charge, and dark current, respectively.

With different voltage at room temperature for the incident THz frequency of 0.1 THz. The R_A linearly increases with

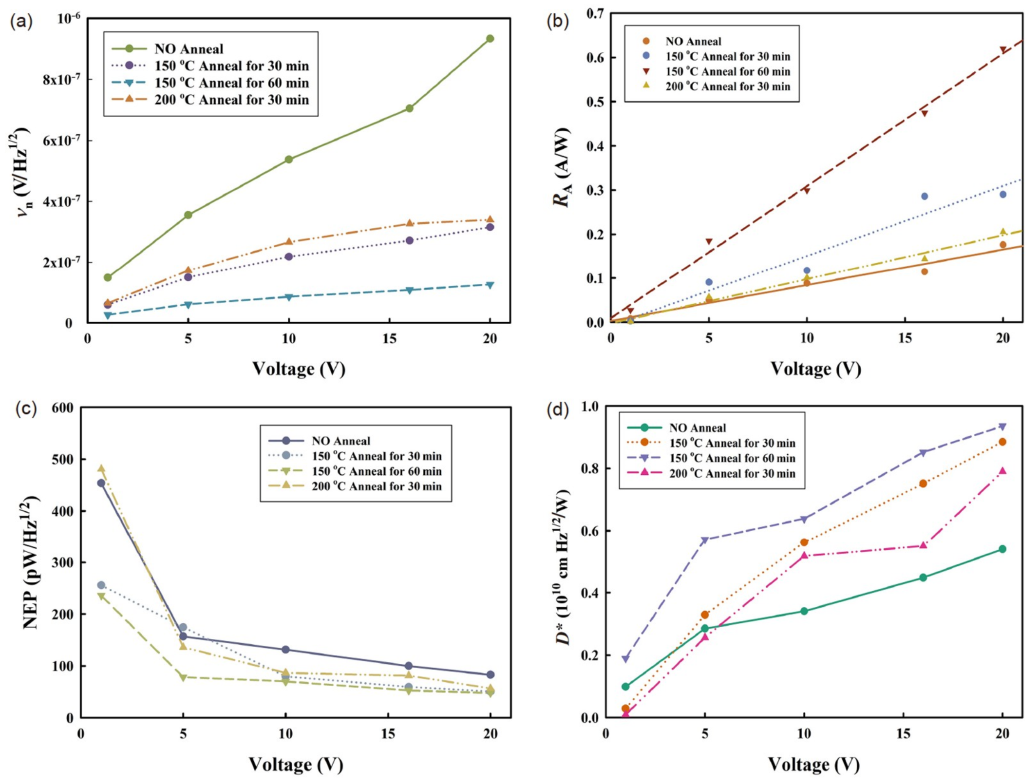

Figure 4 (Color online) Results of terahertz detection performance parameters for WTe_2 films. (a) Device noise. (b) Sensitivity. (c) Equivalent noise power. (d) Detectivity D^*.

the applied voltage, due to the nonequilibrium electrons proportional to the drift velocity. With the applied voltage of 20 V, the R_A for 150°C, 60 and 30 min annealing time devices, and 200°C 30 min annealing time devices are 0.6, 0.3 and 0.21 A/W, which is higher than the unannealed reference devices 0.17 A/W. The NEP are 47.78, 50.55, 56.61 and 82.89 pW/Hz$^{1/2}$. The D^* of the rating and spiral electrode devices are 9.4, 8.8, 7.9, and 5.4 × 10^9 cm Hz$^{1/2}$/W.

3 Results and discussion

We conducted simulations to analyze the surface electric field distribution and surface current distribution of different microstructure arrays for an incident terahertz source at 0.1 THz. The simulation results for devices with spacing of 70 and 140 μm are presented in Figures 5 and 6, respectively. Our results indicate that, for the same 2D pattern but with different spacing, the results demonstrate that when the spacing approaches 100 μm, the superimposed results align more closely with the resonant frequency of the LSP effect. This suggests that devices operating at or near the resonant frequency can effectively confine more terahertz waves due to the enhanced localized equipartition excitonic effects introduced by the microstructure arrays. Consequently, the simulated results reveal stronger surface electric fields. Furthermore, the strength of surface currents reflects the extent of carrier aggregation, and these currents become more pronounced as the microstructure array parameters approach the size of LSP resonance.

Furthermore, when comparing various 2D patterns with the same line spacing, it is observed that the folded line array with 90° angles exhibits a greater number of regions for restricting terahertz waves in comparison to the linear array. In addition to the regions near the lines, the regions associated with each folded angle can also be utilized for limiting terahertz waves. Consequently, the regions available for restricting terahertz waves are more extensive. This observation is supported by the simulation results, which indicate that the folded line microstructure array possesses larger regions for limiting terahertz waves. Moreover, the surface electric field, which is responsible for restricting the strength of the terahertz field, is also larger in the folded line microstructure array. Additionally, the generated surface current is also greater in this array.

Finally, the impact of metal layers is taken into consideration. The metal nanofilm serves two primary functions: Firstly, it forms a microcavity between the active semimetal layer and the Au layer, enhancing the interaction between the incident terahertz waves and the active layer. Crystallized Weyl semi-metal exhibits a stronger ability to absorb low-energy terahertz photons and generate photocurrents.

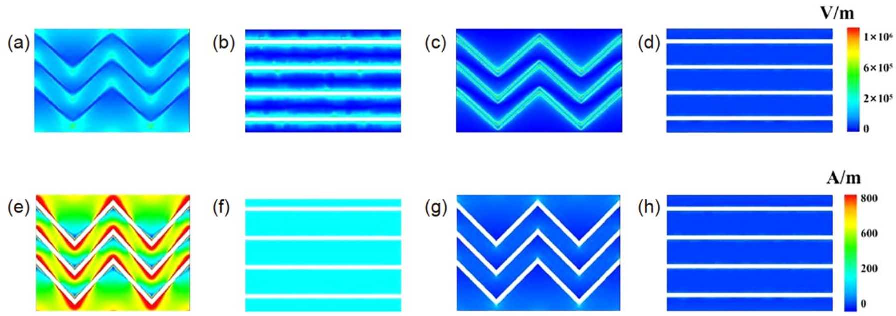

Figure 5 (Color online) Simulation of the device with 70 μm line spacing. (a) Electric field distribution of folded line array with Au nanofilm. (b) Electric field distribution of linear array with Au nanofilm. (c) Electric field distribution of linear array without Au nanofilm. (d) Electric field distribution of linear array without Au nanofilm. (e) Surface current distribution of folded line array with Au nanofilm. (f) Surface current distribution of linear array with Au nanofilm. (g) Surface current distribution of folded array without Au nanofilm. (h) Surface current distribution of linear array without Au nanofilm.

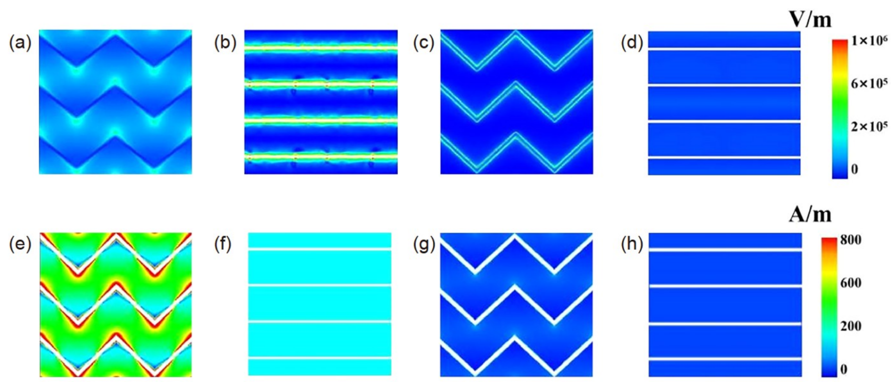

Figure 6 (Color online) Simulation of 140 μm line pitch device. (a) Electric field distribution of folded line array with Au nanofilm. (b) Electric field distribution of linear array with Au nanofilm. (c) Electric field distribution of linear array without Au nanofilm. (d) Electric field distribution of linear array without Au nanofilm. (e) Surface current distribution of folded line array with Au nanofilm. (f) Surface current distribution of linear array with Au nanofilm. (g) Surface current distribution of folded array without Au nanofilm. (h) Surface current distribution of linear array without Au nanofilm.

Additionally, the enhancement of displacement current response near the Weyl point is more significant. Therefore, the introduction of the microcavity structure enhances the efficiency of generating photocurrents in the Weyl semimetal layer. Secondly, the addition of metal nanofilms with subwavelength microstructures creates EIWs at the intersection of the metal and semimetal layers. This structure confines the free carriers in the metal layer to the EIW, greatly increasing the carrier concentration in the semimetal active layer. Consequently, the combination of these two factors explains the confinement effect of the metal layer device on the terahertz field and the significant enhancement of the surface current, as observed in the simulation results. Based on this, we have designed the preferred parameters for a 2D folded array with a 70 μm structural spacing of the Au-plated reflective layer. Since the processing parameters for the crystalline WTe_2 film have been determined, the subsequent experiments are conducted using the preferred WTe_2 crystalline film to fabricate the device. The process involves preparing an Au nanofilm through magnetron sputtering on Si as a reflection layer, followed by the preparation and annealing of WTe_2 at 150°C for 60 min. Finally, an Au electrode layer with an electrode size of 1 mm × 10 mm and a spacing of 3 mm is processed on the device surface.

Figure 7 illustrates the ablated folded line groove array on a thin film-based Si substrate. It consists of the WTe_2 active layer (1.08 μm thick) and the Au reflective layer (36 nm thick), sequentially grown on the Si substrate (400 μm thick). For the laser ablation process, a femtosecond laser with a repetition frequency of 50 kHz, pulse width of 433 fs, average output power of 65 mW, and spot radius of 10 μm is utilized. The exposure time is controlled by an electronic shutter with an on-off time of 0.1 ms, resulting in five pulses at the minimum on-off time. The sample is positioned on a computer-controlled 3D translation stage with a minimum displacement of 20 μm. The scanning speed is precisely controlled to fabricate the desired pattern in the films. The scanning speeds of the 3D stage are 10 and 8 mm/s for the WTe_2 film and the WTe_2 sandwiched Au film, respectively. The detection setup is the same as the one used for the WTe_2 films, as shown in Figure 3(a). The femtosecond laser direct writing achieves a line width of 20 μm.

Figure 8 presents the results of the terahertz detection performance for devices with line spacings of 70 and 140 μm, with and without the Au layer, at room temperature. The R_A, NEP, and D^* are also calculated by comparing the light-dark current to demonstrate the photo-electrical conversion capability of the detectors.

For devices that have varying line spacing, the closer the line spacing and line width are to 100 μm, the closer the size aligns with the resonant frequency of the LSP effect. Consequently, devices that are close to the resonant frequency experience a stronger LSP effect introduced by the microstructured array, resulting in a greater confinement of terahertz waves. The degree of carrier aggregation is reflected in the surface current, which is stronger when the microstructured array parameters are closer to the LSP resonant frequency. This is evident in the higher sensitivity, smaller NEP, and larger D^* values. For devices coated with an Au layer, the engraved microstructure introduces the enhanced internal wave (EIW) effect and the micro-cavity effect reflected from the Au layer. The combination of these two effects significantly enhances the interaction between the device's active layer and the terahertz wave. Additionally, the carrier aggregation effect generated by EIW further enhances the surface carrier concentration. As a result, the detection efficiency increases, leading to a sharp rise in the bright current and higher sensitivity, smaller NEP, and larger D^* values. When subjected to different voltages at room temperature for an incident THz frequency of 0.1 THz, the responsivity (R_A) linearly increases with the applied voltage.

With the applied voltage of 80 V, the R_A of 70 and 140 μm line spacing devices with or without the Au layer are 34 A/W (6.8 MV/W), 17.7 A/W (3.42 MV/W), 6.1 A/W and 3.4 A/W, which is higher than that of a Golay cell (0.1 MV/W). With the applied voltage of 80 V, the NEP is

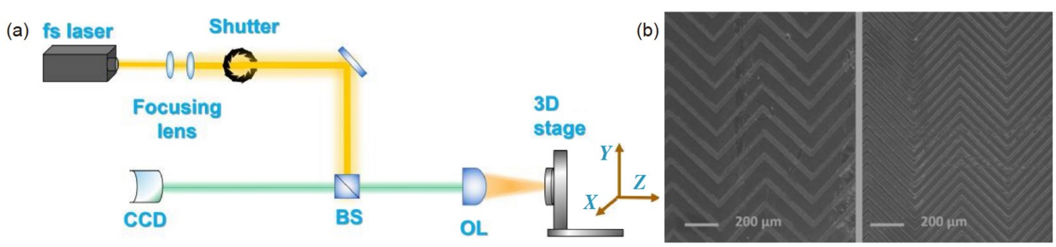

Figure 7 (Color online) Schematic diagram of femtosecond laser direct writing system and sample. (a) Femtosecond laser direct writing processing of the same schematic diagram and (b) the sample picture after processing the pattern (WTe_2 sandwiched Au film). Left: Line spacing of 140 μm; right: Line spacing of 70 μm.

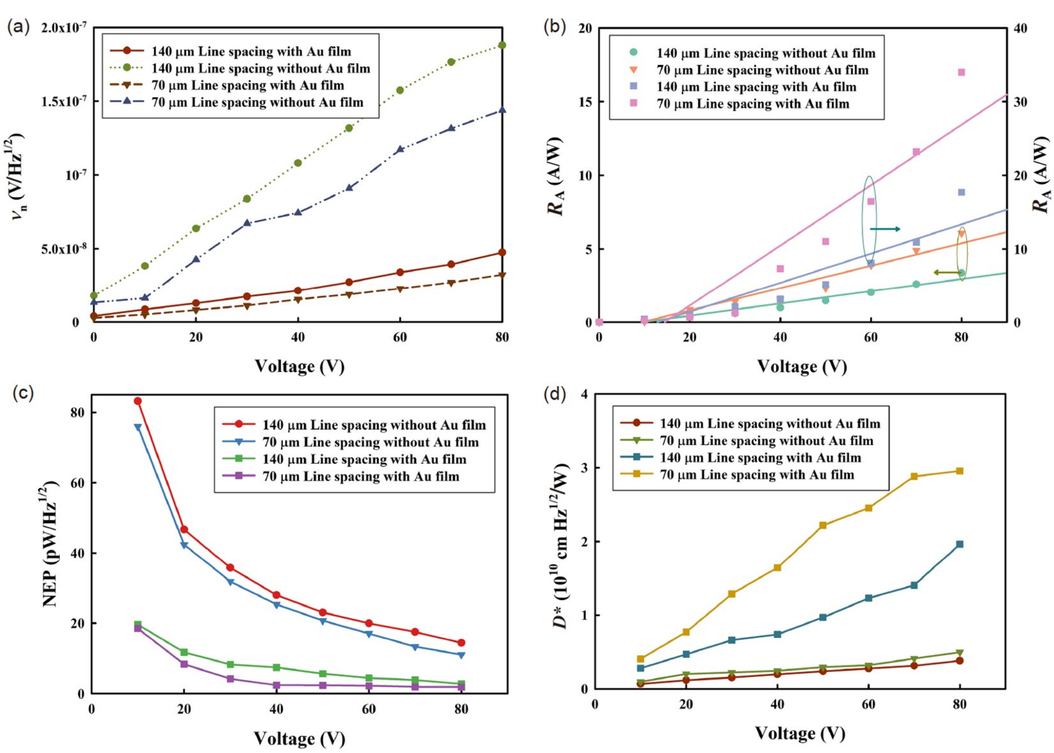

Figure 8 (Color online) Results of terahertz detection performance parameters of the device. (a) Device noise. (b) Sensitivity. (c) Equivalent noise power. (d) Detection rate D^*.

Table 1 Terahertz detectors at room temperature during recent 3 years[a)]

Materials	Frequency	Detection mechanism	R_A	NEP (pW/Hz$^{1/2}$)	Area	Ref.
Bi_2Se_3	0.3 THz	LSP	0.29×10^{-2} V/W	0.36	Nano	[24]
AlGaN/GaN	0.5 THz	FET	10 V/W	25	Nano	[25]
$PtTe_2$	0.12 THz	FET	1400 V/W	10	Nano	[26]
$PdTe_2$	0.3 THz	PCE	1.3×10^{-8} V/W	57	Nano	[27]
Black phosphorus	0.29 THz	PTE	297 V/W	138	Nano	[28]
InSb	0.03 THz	SPP	2.6×10^5 V/W	0.02	Micron	[22]
Golay cell (Commercial)	0.1 THz	Thermal	1×10^5 V/W	140	Millimetre	[29]
Bolometer (Commercial)	0.1 THz	Thermal	2.4×10^5 V/W (4.2 K)	0.25	Millimetre	[30]
PbS micro-wheel array	0.28 THz 0.14 THz	LSP	4.56 A/W 3.12 A/W	0.0188 0.661	Millimetre	[23]
WTe_2 microdisk array	0.1 THz	LSP	8.78 A/W	0.74	Millimetre	[31]
$MoTe_2$ nanofilm	0.1 THz	PCE	4 A/W	9.74	Millimetre	[32]
Te	0.305 THz	PCE	9.83 A/W	0.6	Nano	[33]
$Bi_{88}Sb_{12}$	0.14 THz	Thermoelectric	12–20 mV/W	770	Micron	[34]
GO-Bi	0.22 THz	Thermoelectric	0.226 V/W	1330	Micron	[35]
SiGe	0.9 THz	HBT	0.65 A/W	19	Nano	[36]
AlGaN/GaN	0.74 THz	HEMTs	0.56 A/W	–	Micron	[37]
WTe_2 crystalline film direct-write devices	0.1 THz	EIW/LSP/Micro-cavity	34 A/W or 6.8×10^5 V/W	1.8	Millimetre	This work

a) PCE: Photoconductive effect; EIW: Electromagnetic induction well; PTE: Photothermoelectirc; FET: Field effect transistor; SPP: Surface plasmon polariton; LSP: Localized surface plasmon; HEMTs: High-electron-mobility transistors; HBT: Heterojunction bipolar transistor.

1.8, 2.7, 11.1 and 14.3 pW/Hz$^{1/2}$ for the 70 and 140 μm line spacing devices with the Au layer which just 1/50 to 1/77 of the commercial Golay cell (140 pW/Hz$^{1/2}$) [26]. The D^* of the rating and spiral electrode devices are 2.95×10^{10}, 1.96×10^{10}, 0.49×10^{10} and 0.38×10^{10} cm Hz$^{1/2}$/W at the applied voltage of 80 V.

The response rate of devices with line spacing of 70 μm, with or without an Au nanofilm, was tested and yielded current response times of 80 and 93 ms, respectively. For devices with line spacing of 140 μm, with or without an Au nanofilm, the response times were 103 and 115 ms. It can be observed that the response time decreases as the line spacing decreases, indicating reduced carrier diffusion freedom in the plane. Additionally, the presence of the Au film enhances carrier concentration on the device surface, resulting in shorter response times.

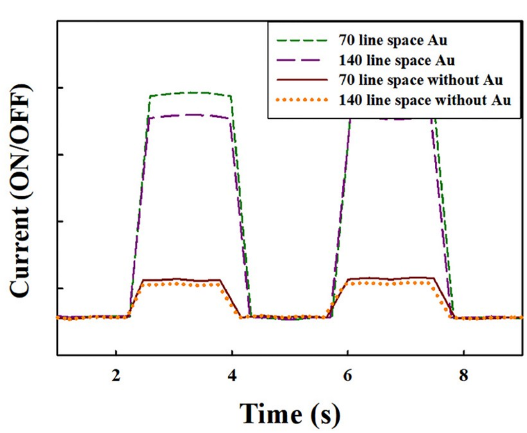

Figure 9 (Color online) Response time test chart of the four devices.

Based on the advantages of reproducibility, mass production and high-efficiency detection at room temperature, we have compared terahertz detectors in the past three years, taking into account factors such as preparation and detection performance (responsivity and equivalent noise power). Our proposed solution involves a microcavity structure comprising an annealed crystalline Weyl-semimetallic active layer and an Au nano-layer, along with an additional sub-wavelength structure to introduce EIW and LSP effects. This combination enhances the device's responsiveness to 6G signals, providing an effective and significant solution for high-performance terahertz detection technology.

4 Conclusion

To meet the demand for ultra-sensitive detectors for 6G IoT edge intelligence technology, we prepared large-area Weyl-semimetal layers by magnetron sputtering, obtained high-quality Weyl-semimetal active layers by controlled annealing conditions, and then prepared thin Au layers as micro-cavity reflection layers, processed 2D microstructure patterns by femtosecond laser direct writing technology, and introduced both EIW and LSP. The detection sensitivity is 34 A/W for the preferably processed 36 nm Au film and 150°C, 1 h annealing time of WTe_2 film, 90° folding line with a fixed line width of 20 μm and a line spacing of 70 μm. The equivalent noise power NEP is 1.8 $pW/Hz^{1/2}$ and the response time is 80 ms. The proposed scheme offers the potential to manufacture high-performance terahertz detectors with industrial production potential proposed and provides an effective technical solution for the development of 6G technology.

This work was supported by the National Natural Science Foundation of China (Grant No. 12104314) and the Key Laboratory of Optoelectronic Devices Systems of Ministry of Education and Guangdong Province and Research Foundation of Liaocheng University (Grant No. 318052316).

1 Qi F, Li W J, Yu P, et al. Deep learning based BackCom multiple beamforming for 6G UAV IoT networks. Eurasip J Wirel Comm, 2021, 50
2 Liao S, Wu J, Li J, et al. Information-centric massive IoT-based ubiquitous connected VR/AR in 6G: A proposed caching consensus approach. IEEE Internet Things J, 2021, 8: 5172–5184
3 Gupta R, Reebadiya D, Tanwar S. 6G-enabled edge intelligence for ultra-reliable low latency applications: Vision and mission. Comput Standards Interfaces, 2021, 77: 103521
4 Qi W, Li Q, Song Q, et al. Extensive edge intelligence for future vehicular networks in 6G. IEEE Wireless Commun, 2021, 28: 128–135
5 Guo H, Zhou X, Liu J, et al. Vehicular intelligence in 6G: Networking, communications, and computing. Vehicular Commun, 2022, 33: 100399
6 Talwar S, Himayat N, Nikopour H, et al. 6G: Connectivity in the era of distributed intelligence. IEEE Commun Mag, 2021, 59: 45–50
7 Huang X, Zhang K, Wu F, et al. Collaborative machine learning for energy-efficient edge networks in 6G. IEEE Network, 2021, 35: 12–19
8 Liu D F, Liang A J, Liu E K, et al. Magnetic Weyl semimetal phase in a Kagomé crystal. Science, 2019, 365: 1282–1285
9 Rees D, Manna K, Lu B, et al. Helicity-dependent photocurrents in the chiral Weyl semimetal RhSi. Sci Adv, 2020, 6: eaba0509
10 Morali N, Batabyal R, Nag P K, et al. Fermi-arc diversity on surface terminations of the magnetic Weyl semimetal $Co_3Sn_2S_2$. Science, 2019, 365: 1286–1291
11 Wang Z Y, Cheng X C, Wang B Z, et al. Realization of an ideal Weyl semimetal band in a quantum gas with 3D spin-orbit coupling. Science, 2021, 372: 271–276
12 Sie E J, Nyby C M, Pemmaraju C D, et al. An ultrafast symmetry switch in a Weyl semimetal. Nature, 2019, 565: 61–66
13 He H, Qiu C, Ye L, et al. Topological negative refraction of surface acoustic waves in a Weyl phononic crystal. Nature, 2018, 560: 61–64
14 Wang Z, Wieder B J, Li J, et al. Higher-order topology, monopole nodal lines, and the origin of large Fermi arcs in transition metal dichalcogenides XTe_2 (X=Mo, W). Phys Rev Lett, 2019, 123: 186401
15 Sadowski J, Domagała J Z, Zajkowska W, et al. Structural properties of TaAs Weyl semimetal thin films grown by molecular beam epitaxy on GaAs(001) substrates. Cryst Growth Des, 2022, 22: 6039–6045
16 Wang Y, Wang Q, Wang Q, et al. Dynamically adjustable-induced THz circular dichroism and biosensing application of symmetric silicon-graphene-metal composite nanostructures. Opt Express, 2021, 29: 8087–8097
17 Zhong M. Simulation and fabrication of a single-band tunable absorber in 20–50 THz range based on cross array metamaterials. Infrared Phys Tech, 2020, 107: 103322
18 Zhong M, Jiang X, Zhu X, et al. Design and measurement of a single-dual-band tunable metamaterial absorber in the terahertz band. Physica E-Low-dimensional Syst NanoStruct, 2020, 124: 114343
19 Liu N, Wang Y, Li W B, et al. Thermal stability study of Weyl semimetal WTe_2/Ti heterostructures by Raman scattering. Acta Phys Sin, 2022, 71: 197501
20 Lu W, Zhang Y, Zhu Z, et al. Thin tungsten telluride layer preparation by thermal annealing. Nanotechnology, 2016, 27: 414006
21 Song Q, Chen H, Zhang M, et al. Broadband electrically controlled bismuth nanofilm THz modulator. APL Photonics, 2021, 6: 056103
22 Tong J, Suo F, Zhang T, et al. Plasmonic semiconductor nanogroove array enhanced broad spectral band millimetre and terahertz wave detection. Light Sci Appl, 2021, 10: 58
23 Song Q, Xu Y, Zhou Z, et al. Terahertz detectors for 6G technology using quantum dot 3D concave convergence microwheel arrays. ACS Photonics, 2022, 9: 2520–2527
24 Tang W, Politano A, Guo C, et al. Ultrasensitive room-temperature terahertz direct detection based on a bismuth selenide topological insulator. Adv Funct Mater, 2018, 28: 1801786
25 Bauer M, Ramer A, Chevtchenko S A, et al. A high-sensitivity AlGaN/GaN HEMT terahertz detector with integrated broadband bow-tie antenna. IEEE Trans THz Sci Technol, 2019, 9: 430–444
26 Xu H, Guo C, Zhang J, et al. $PtTe_2$-based type-II Dirac semimetal and its van der Waals heterostructure for sensitive room temperature terahertz photodetection. Small, 2019, 15: 1903362
27 Guo C, Hu Y, Chen G, et al. Anisotropic ultrasensitive $PdTe_2$-based phototransistor for room-temperature long-wavelength detection. Sci Adv, 2020, 6: eabb6500
28 Guo W, Dong Z, Xu Y, et al. Sensitive terahertz detection and imaging driven by the photothermoelectric effect in ultrashort-channel black phosphorus devices. Adv Sci, 2020, 7: 1902699
29 Terahertz detector Golay cell product introduction and specific parameters, http://www.eachwave.com/Product/054637111.html (2022-02-14) [ACCESS 2023-07-27]
30 Terahertz detector bolometer product introduction and specific parameters, http://www.eachwave.com/Product/456031513.html (2022-02-14) [ACCESS 2023-07-27]
31 Song Q, Zhou Z, Zhu G, et al. Microdisk array based Weyl semimetal nanofilm terahertz detector. Nanophotonics, 2022, 11: 3595–3602
32 Zhou Z, Song Q, Xu Y, et al. Magnetron sputtering deposited large-scale Weyl semimetal THz detector. Infrared Phys Tech, 2022, 121: 104060
33 Ma W, Gao Y, Shang L, et al. Ultrabroadband tellurium photoelectric detector from visible to millimeter wave. Adv Sci, 2022, 9: 2103873
34 Khodzitsky M, Tukmakova A, Zykov D, et al. THz room-temperature detector based on thermoelectric frequency-selective surface fabricated from $Bi_{88}Sb_{12}$ thin film. Appl Phys Lett, 2021, 119: 164101
35 Jia H, Tang X, Zhu X, et al. Low-noise room-temperature terahertz detector based on the photothermoelectric effect of graphene oxide-Bi films. Optical Mater, 2023, 136: 113432
36 Andree M, Grzyb J, Jain R, et al. Broadband modeling, analysis, and characterization of SiGe HBT terahertz direct detectors. IEEE Trans Microwave Theor Techn, 2022, 70: 1314–1333
37 Quach P, Jollivet A, Babichev A, et al. A 5.7 THz GaN/AlGaN quantum cascade detector based on polar step quantum wells. Appl Phys Lett, 2022, 120: 171103